HAL open science

Texture Analysis Based Damage Detection of Ageing Infrastructural Elements

Michael O'Byrne, Franck Schoefs, Bidisha Gosh, Vikram Pakrashi

▶ To cite this version:

Michael O'Byrne, Franck Schoefs, Bidisha Gosh, Vikram Pakrashi. Texture Analysis Based Damage Detection of Ageing Infrastructural Elements. Computer-Aided Civil and Infrastructure Engineering, 2013, 28 (3), pp.162-177. 10.1111/j.1467-8667.2012.00790.x . hal-01007357

HAL Id: hal-01007357
https://hal.science/hal-01007357v1

Submitted on 16 Jun 2014

HAL is a multi-disciplinary open access archive for the deposit and dissemination of scientific research documents, whether they are published or not. The documents may come from teaching and research institutions in France or abroad, or from public or private research centers.

L'archive ouverte pluridisciplinaire HAL, est destinée au dépôt et à la diffusion de documents scientifiques de niveau recherche, publiés ou non, émanant des établissements d'enseignement et de recherche français ou étrangers, des laboratoires publics ou privés.

Distributed under a Creative Commons Attribution 4.0 International License

Texture Analysis Based Damage Detection of Ageing Infrastructural Elements

Michael O'Byrne

Department of Civil, Structural and Environmental Engineering, Trinity College Dublin, Dublin, Ireland

Franck Schoefs

LUNAM Université, Université de Nantes-Ecole Centrale de Nantes-CNRS, GeM, Institute for Research in Civil and Mechanical Engineering, University of Nantes, Nantes, France; IXEAD/CAPACITES Society, Nantes, France

Bidisha Ghosh

Department of Civil, Structural and Environmental Engineering, Trinity College Dublin, Dublin, Ireland

&

Vikram Pakrashi

Department of Civil and Environmental Engineering, University College Cork, Cork, Ireland

Abstract: *To make visual data a part of quantitative assessment for infrastructure maintenance management, it is important to develop computer-aided methods that demonstrate efficient performance in the presence of variability in damage forms, lighting conditions, viewing angles, and image resolutions taking into account the luminous and chromatic complexities of visual data. This* article *presents a semi-automatic, enhanced texture segmentation approach to detect and classify surface damage on infrastructure elements and successfully applies them to a range of images of surface damage. The approach involves statistical analysis of spatially neighboring pixels in various color spaces by defining a feature vector that includes measures related to pixel intensity values over a specified color range and statistics derived from the Grey Level Co-occurrence Matrix calculated on a quantized grey-level scale. Parameter optimized nonlinear Support Vector Machines are used to classify the feature vector. A Custom-Weighted Iterative model and a 4-Dimensional Input Space model are introduced. Receiver Operating Characteristics are employed to assess and enhance the detection efficiency under various damage conditions.*

1 INTRODUCTION

The deteriorating condition of infrastructure worldwide and the excessive costs required for reparative work necessitate the invention of efficient and effective detection techniques. Recent estimates suggest that $1.6 trillion dollars will be needed for rehabilitation, replacement, and maintenance of current infrastructure systems with the next 20 years for the United States alone (Adeli and Jiang, 2009). With this in mind, it is vital that a comprehensive strategy for the periodic inspection and monitoring of structures (Schoefs et al., 2011; Lajnef et al., 2011; Gangone et al., 2011) is developed beginning from the construction phase. This is even more relevant given the increased loads and ever challenging environmental conditions that structures are faced with (Cusson et al., 2011; Xia et al., 2011). Non-Destructive Testing (NDT) techniques are frequently used for the inspection process as they often offer the only practical means for detecting the presence of damage and quantifying its severity. The information obtained from NDT techniques may be used to better understand damage mechanisms such as initiation and propagation. Identifying these factors allows for improved estimates of the remaining service life which leads to a more reliable Infrastructure Management System (IMS) (Rong-Yau et al., 2010). A reliable IMS can help the decision makers to optimize intervention strategies and enable them to make informed decisions regarding the future course of action that would maximize the potential of their investments. This aspect has attracted a growing interest in recent years as the importance of life cycle optimization and the related financial benefits continue to be recognized (Sarma and Adeli, 1998; Sirca and Adeli, 2005). For a well calibrated IMS, it is important that the input information from an NDT technique is accurate and comprehensive. The measure of the onsite performance of a NDT tool remains a pertinent question in the majority of cases (Schoefs et al., 2012a). The most suitable NDT for a given application will largely depend on the damage to be detected and will require an in-depth knowledge of the advantages and limitations associated with each option.

There exists a broad range of NDT techniques to choose from. NDT techniques may be partitioned into two categories: non-visual and visual based techniques. Among the non-visual NDT techniques are ultrasonic scanning (Iyer et al., 2005), surface wave simulation (Kim and Kwak, 2008), acoustic emission techniques (Sohn et al., 2008; Li et al., 2011a), ground penetrating radar (Belli et al., 2008), eddy current testing (Yusa et al., 2006), as well as a lot of recent interest in vibration based techniques (Cruz and Salgado, 2009; Adewuyi and Wu, 2011; Jafarkhani and Masri, 2011; Li et al., 2011b; Talebinejad et al., 2011). There are several specialist visual techniques such as remote visual inspection (Nugent and Pellegrino, 1991) and laser based scanners (Mei et al., 2004; Park et al., 2007), etc., yet the most common visual based approach is standard visual inspections carried out by trained engineers.

Visual inspections performed by trained engineers involve significant qualitative and some limited quantitative assessments. The quality of the assessment largely depends on the ability of the inspectors to observe and objectively record details of defects. However, this approach is prone to considerations such as operator boredom, lapses in concentration, subjectivity, and fatigue. These aspects contribute to the variability and reduced accuracy of visual inspections (Agin, 1980; Komorowski and Forsyth, 2000). Furthermore, there is no agreed protocol of collection and subsequent interpretation of visual information despite playing a central role in any infrastructure maintenance management framework. One feature of visual inspections that does remain constant is that the inspections are almost always accompanied with the creation of an image archive. However, there exist very few techniques that fully exploit these images in either a qualitative or quantitative fashion. Employing an image processing based approach in conjunction with traditional visual inspection techniques seems like a natural partnership given that photographing damaged regions is already a widely embraced practice for visual inspections. The primary advantages associated with image processing offset some of the limitations of visual inspections. Image processing based detection of damages offers a far greater reproducible and measurable performance over visual inspection techniques (Gallwey and Drury, 1986). Additionally, it enables a quantitative assessment of the current extent of damage, as well as offering an accurate assessment of degradation over time by analyzing archived images.

Some examples of application of image processing algorithm in visual detection of damages have been developed by researchers in the field of pipe engineering (Iyer and Sinha, 2006; Tsai and Huang, 2010), concrete crack detection (Nishikawa et al., 2012), and road materials (Cord and Chambon, 2011). However, the image based segmentation techniques are far from being fully exploited in the field of NDT. This article presents a semi-automatic image based technique for detection and classification of damaged regions in images of infrastructural elements using texture as the basis for segmentation. The image segmentation algorithm is unique in including information derived from Grey Level Co-occurrence Matrix (GLCM) based on a quantized grey-level scale along with statistical and energy information from the pixel intensity values based on a predefined range [0,255] to form a feature vector representing the texture characteristics of the image and consequent classification of such feature vectors from all parts of the image to identify damaged region through non-linear Support Vector Machines (SVM) models.

Texture is an innate property of surfaces (Haralick et al., 1973) which can be utilized to identify damaged regions on infrastructural elements which typically have differing textures compared to the undamaged surfaces. For human observers, texture may be qualified by terms, such as fine, coarse, smooth, rippled, molled, irregular, or lineated (Haralick et al., 1973). From a computational perspective, quantifying the perceived texture in an image is significantly more challenging. There are numerous texture based techniques which attempt to characterize texture: wavelet analysis (Lu et al., 1997), Laws' texture energy (Choi et al., 2011), First-Order Statistics (FOS) (Gill, 1999), and GLCM

(Gadelmawla, 2004). This article adopts a GLCM approach in conjunction with FOS. The use of GLCM statistics in conjunction with first order descriptive statistics has been employed before by Abbiramy and Tamilarasi (2011) in the field of medical imaging to detect abnormalities in human spermatozoa. Their approach entailed a pre-processing stage involving noise reduction, followed by the calculation of 15 GLCM statistics coupled with four first-order descriptive statistics from converted grey-scale images. GLCM and FOS statistics formed part of a larger feature vector that was also populated with nine additional morphological features. The authors used a single feature vector assigned to the overall image which was later classified through a neural network structure. The proposed technique in this article extends this image classification study to a color image segmentation algorithm incorporating a number of original aspects that are particularly advantageous to the chosen application.

The proposed technique involves a unique set of texture measures that are calculated at every pixel in an image using a sliding window approach. Four GLCM statistics are calculated based on a quantized grey-level scale with 8 levels. These are: Angular Second Moment (ASM), homogeneity, contrast, and correlation. Six FOS and energy information features are calculated directly from the pixel intensity values which are based on a predefined range [0,255]. These are: Shannon entropy, mean, variance, range, skewness, and kurtosis. The quantized range adopted for the GLCM statistics avoids formation of sparse matrices during computation, leading to a faster detection. The wider range adopted for the FOS and Shannon entropy offers more sensitivity allowing for more accurate and representative features to be extracted.

Non-linear SVM models are used to classify pixels as either damaged or undamaged based on the feature vector. Although GLCM had been used previously in conjunction with SVM classification (Ben Salem and Nasri, 2010; Xian, 2010), the approach in this article introduces two new SVM classification models; a Custom-Weighted Iterative (CWI) model and a four-dimensional input space (4DIS) model in which the feature vectors were mapped to a 4DIS. This article also presents a Receiver Operating Characteristics (ROC) based framework for parameter optimization. The parameter optimization procedure involved measuring the performance of an SVM classifier for a given pair of parameters using the α-δ method (Schoefs et al., 2012b) and adjusting the parameters accordingly until suitably optimized. The proposed technique was evaluated in various color spaces (Red–Green–Blue (RGB), Hue-Saturation-Value (HSV), and $L^*a^*b^*$) to determine the best segmentation space.

The following section details the methodology of the proposed technique. The proposed methodology is evaluated through the identification of six disparate damage types from six different images of ageing infrastructural elements under different lighting and environmental conditions. Section 3 evaluates the performance of the SVM classification models applied to each image in each color space. Section 4 concludes the article.

2 METHODOLOGY

An image based damage detection algorithm has been proposed in this article. The algorithm involves two steps; the first step is to develop a texture characteristics map of a color image. The map has been developed using feature vector for each pixel following the method described in Section 2.1. The second step is to classify the damaged regions in the image using SVM as described in Section 2.2. The methodology is illustrated in the following flowchart (Figure 1).

2.1 Texture characteristics map

A texture characteristics feature vector $\{v_f\}_{a,b,c}$ has to be generated for each pixel within the original image, I, for each color channel, c, where f indicates the index of the vector element and (a,b) indicates the spatial coordinates of the pixel. The first four elements of $\{v_f\}_{a,b,c}$ are obtained by computing statistics derived from a GLCM. These statistics are ASM, homogeneity, contrast, and correlation. The GLCM is primarily calculated for grey images yet may be readily extended to individual color channels. The remaining six first-order texture features are based on measures calculated from the original pixel values mapped over a range of $[0, 255]$. These features are Shannon entropy, mean, variance, range, skewness, and kurtosis.

The feature vector for each pixel is calculated separately for each color channel and can be combined together to form a four-dimensional array. The feature vector is generated for each pixel using a sliding window, SW, that moves throughout the image and provides the basis for the GLCM statistics and the distributions used for calculating descriptive statistics and Shannon entropy. The window started at the top left-hand corner of the image and horizontally moved in steps of one pixel until it reached the end of a row, at which point it progressed onto the leftmost point in the next row. The center is indicated as (a,b) and the size of the window (N-pixel $\times$ N-pixel) is optimized for best performance. A trial and error approach is used to determine the optimal size. The optimal size of SW is not necessarily the one which most effectively describes the

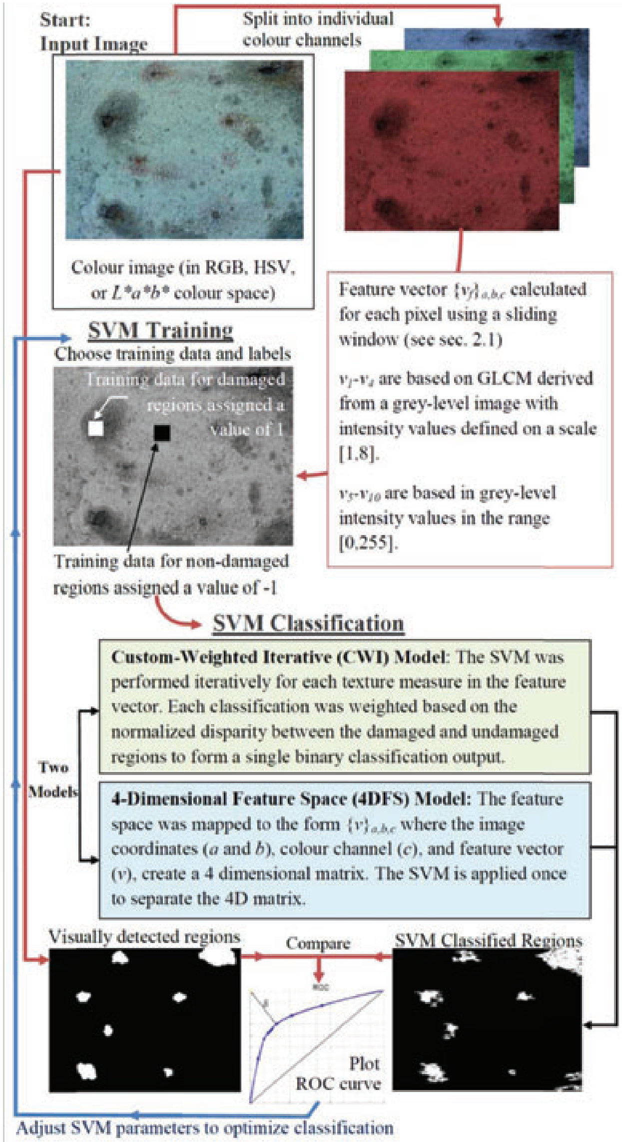

Fig. 1. Methodology Flowchart.

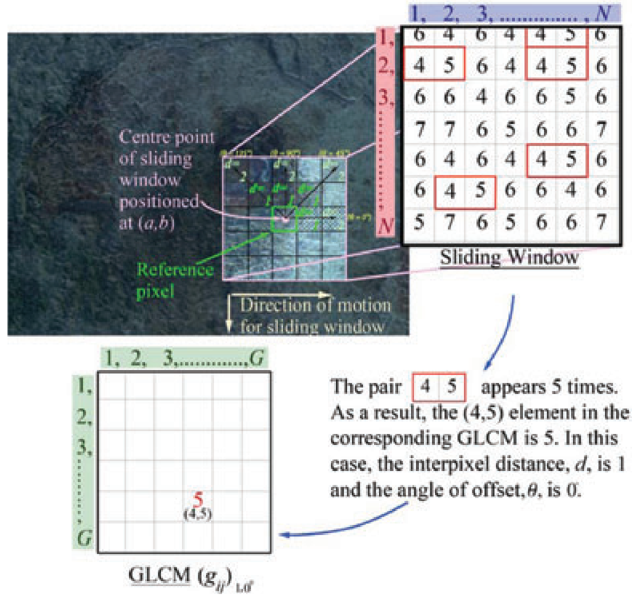

Fig. 2. Overview of the GLCM process.

textural composition of one region, but the one which provides the best differentiation between damaged and undamaged zones which have distinct textures. This optimization step may be worthwhile if large batches of images featuring similar damaged surfaces are being processed. It was experimentally found, however, that the classification accuracy of the technique was not overly sensitive to the window size. Similarly, the computational time of the technique was not significantly affected by the size of *SW*. An increase in the size of *SW* was accompanied by a marginal increase in the overall computational time. In this article, a nominal window size of 10×10 square pixels was used.

2.1.1 GLCM features. The process in which the GLCM is created is illustrated in Figure 2.

The GLCM is a matrix of frequency values of paired combinations of pixel intensities as they appear in certain specific spatial arrangements within an image or sub-image. The GLCM for each pixel is generated through a sub-image that is a sliding window, *SW*, centred on the pixel. Combinations of various pixel pairs within *SW* were counted and the resulting total was assigned to the g_{ij}, in the GLCM which corresponds to the spatial arrangement of the pixel pairs being summated. The spatial indices i and j of the GLCM match the grey level in the reference pixel and the destination pixel, respectively. The spatial arrangement of the reference pixel and destination pixel in relation to each other in *SW* are governed by two parameters: the interpixel distance, d, and the angle of offset, θ. The grey levels are defined using integer values between 1 and G. In this article, the grey levels are defined on a scale of 1–8 ($G = 8$) instead of a larger scale such as [0,255]. Quantizing in this manner increases computational parsimony at the expense of making the GLCM less sensitive to minute fluctuations in pixel intensity values within the sliding window. Despite this reduced sensitivity, the discrimination capabilities of the GLCM remain largely unperturbed as perceivable changes in intensity values between neighboring pixels continue to be taken into account, thus creating condensed yet still descriptive matrices. An illustrated example of the creation process for a GLCM is presented in Figure 2. In this example, the number of occurrences of pixels with a quantized grey level of 4 and 5 appearing horizontally alongside each other in the sliding window ($d = 1$ and $\theta = 0°$) are computed. The number of occurrences of this pair is then assigned to the (4, 5) element in the GLCM corresponding to the chosen value of d and θ. It was experimentally found that paired combinations of intensity values of pixels that are spatially neighboring tend to be more relevant than combinations that involve spatially distant pixels. Accordingly, a value of 1 was chosen for d to ensure a certain level of spatial proximity. The angle along which the interpixel distance was counted, was defined as the angles of offset and the four angles for the offset that were chosen are, $\theta = 0°$, $\theta = 45°$, $\theta = 90°$, $\theta = 135°$. So, this generated a set of 4 GLCMs ($d = 1$; $\theta = 0°, 45°, 90°, 135°$) for each color channel at each pixel.

The GLCM for each pixel is populated as:

$$(g_{ij})_{d,\theta} = \sum_{u=1}^{N}\sum_{z=1}^{N} A \text{ where } A = \begin{cases} 1 \text{ if } s_{uz} = i \text{ and } s_{uz}^{d,\theta} = j \\ 0 \quad \text{otherwise} \end{cases} \tag{1}$$

where s_{uz} is the pixel intensity expressed in quantized grey levels for the reference pixel located at row u and column z within the sliding window; $s_{uz}^{d,\theta}$, is the pixel intensity expressed in quantized grey levels for the destination pixel located at an interpixel distance d along an angle θ from the reference pixel. The GLCMs are normalized as:

$$p(i,j)_{d,\theta} = \frac{(g_{ij})_{d,\theta}}{N(N-1)} \tag{2}$$

The following four texture features are determined from the GLCM:

Angular Second Moment (ASM) represents the uniformity of distribution of grey level in the image.

$$(v_{f=1})_{d,\theta} = \sum_{i=1}^{G}\sum_{j=1}^{G}\{p(i,j)_{d,\theta}\}^2 \tag{3}$$

v_1 ranges from $1/G^2$ to 1. A value of 1 indicates a uniform image.

Homogeneity gives a measure of the similarity of grey levels in the image.

$$(v_{f=2})_{d,\theta} = \sum_{i=1}^{G}\sum_{j=1}^{G} m \cdot p(i,j)_{d,\theta} \text{ where } m = |i-j| \tag{4}$$

v_2 ranges from 0 to G-1. A value of 0 indicates a strong similarity of grey levels in the image.

Contrast is a measure of the local variations present in an image. If there is a high amount of variation the contrast will be high.

$$(v_{f=3})_{d,\theta} = \sum_{m=0}^{G-1} m^2 \left\{\sum_{i=1}^{G}\sum_{j=1}^{G} p(i,j)_{d,\theta}\right\} \tag{5}$$

v_3 ranges from 0 to $(G\text{-}1)^2$. A value of 0 indicates a uniform image.

Correlation is a measure of the grey level linear-dependencies in an image. Correlation will be high if an image contains a considerable amount of linear structure.

$$(v_{f=4})_{d,\theta} = \sum_{i=1}^{G}\sum_{j=1}^{G} \frac{(ij)p(i,j)_{d,\theta} - \bar{\mu}_1\bar{\mu}_2}{\sigma_1\sigma_2} \tag{6}$$

where $\bar{\mu}_1$, $\bar{\mu}_2$, σ_1, and σ_2 are the means and standard deviations of the marginal probability matrices, P_1 and P_2, obtained by summing the rows and columns of $p(i,j)_{d,\theta}$, respectively. v_4 ranges from −1 to 1. A value of 1 indicates a perfectly positively correlated image. An undefined value is returned in the case of a uniform image.

2.1.2 Descriptive statistics and Shannon entropy. The feature vector was further populated by considering five descriptive statistics of the pixel intensity values, along with Shannon entropy. These six features were derived for each pixel using the same sliding window approach employed to calculate the GLCM features. Unlike the GLCM approach, the intensity values used in the distribution adopted the scale [0,255] for several reasons. First, the nature of the statistics generated directly from the intensity values differed from that of the GLCM statistics as it was the magnitude of the intensity values that was considered and not their frequency of occurrence. As such, it was more important for the intensity values to contain as much information as possible which required them to be accurately and precisely defined. Having a bigger sample space provided more sensitive information for characterizing texture. Conversely, the GLCM statistics produced more meaningful results by having similar intensity values grouped together as separately counting perceptually close values may understate their prominence in the sliding window. Secondly, the number of grey-levels employed in the GLCM generation stage directly affected the size of the GLCM, which in turn affected the computational time of the algorithm. The intermediate GLCM generation stage already accounted for a significant portion of the algorithm time so for this reason it was desirable to keep the size of the GLCM to a minimum. Employing quantized intensity values for the descriptive statistics and Shannon entropy on the other hand resulted in no benefits in terms of increased computational efficiency.

A key point to note is that the range of intensity values differed for various color channels. To ensure equality and compatibility, a standardization procedure was employed which linearly scaled the original pixel intensity value $I_{a,b,c}$ in each plane to a new pixel intensity,

$I'_{a,b,c}$, such that it was in the range [0,255] as per:

$$I'_{a,b,c} = 255 \times \frac{I_{a,b,c} - \min(I_{a,b,c})}{\max(I_{a,b,c}) - \min(I_{a,b,c})} \quad (7)$$

This standardization procedure was necessary as the customary range of values in some color channels would be less conducive to statistical analysis. For instance, the typical range for the a^* and b^* channels in the $L^*a^*b^*$ color space is [−128,128]. Proceeding with this range would lead to the Shannon entropy producing meaningless and undefined results for all distributions that had values in the bottom half of the range, [−128,0]. Using scaled pixel intensity values in the sliding window, denoted by $\tilde{s}_{uz}$, avoids this problem.

As with the GLCM based statistics, each of the FOS in the feature vector describes some aspect of the textural composition in a sliding window. The meaning and contribution of each statistic is discussed. Shannon entropy, v_5, is a statistical measure of the uncertainty associated with a random variable.

$$(v_{f=5}) = -\sum_{u=1}^{N}\sum_{z=1}^{N} \tilde{s}_{uz} \log_2 \tilde{s}_{uz} \quad (8)$$

v_5 ranges from $-(N^2 \max(\tilde{s}_{uz}) \log_2(\max(\tilde{s}_{uz})))$ to infinity, which for a pixel intensity range of [0,255] becomes $[-2039\,N^2,\infty]$.

Mean gives the arithmetic average of the intensity values in a window.

$$(v_{f=6}) = \frac{1}{N^2}\sum_{u=1}^{N}\sum_{z=1}^{N} \tilde{s}_{uz} \quad (9)$$

v_6 can range from the minimum value of $\tilde{s}_{uz}$, 0, to maximum value of $\tilde{s}_{uz}$, 255.

Variance is a measure of how far a set of numbers is spread out from the mean.

$$(v_{f=7}) = \frac{1}{N^2}\sum_{u=1}^{N}\sum_{z=1}^{N} (\tilde{s}_{uz} - v_6)^2 \quad (10)$$

v_7 ranges from 0 to $\frac{(\max(\tilde{s}_{uz}) - \min(\tilde{s}_{uz}))^2}{4}$, which equates to 1.625×10^4 for the [0,255] range.

Range gives the difference between the maximum and minimum intensity values in the distribution:

$$(v_{f=8}) = \max(\tilde{s}_{uz}) - \min(\tilde{s}_{uz})\ \forall(u, z) \quad (11)$$

Skewness is a measure of the asymmetry of the data around the sample mean.

An estimate for the skewness is

$$(v_{f=9}) = \frac{1}{v_7^{3/2}}\sum_{u=1}^{N}\sum_{z=1}^{N} (\tilde{s}_{uz} - v_6)^3 \quad (12)$$

v_9 ranges from $-\infty$ to ∞.

Kurtosis is a measure of the peakedness of a distribution. A positive value for kurtosis indicates that the distribution has a greater peakedness than that predicted by a normal distribution, although a negative value indicates that the distribution is less peaked than predicted by a normal distribution.

An estimate for the kurtosis is given by

$$(v_{f=10}) = \frac{1}{v_7^2}\sum_{u=1}^{N}\sum_{z=1}^{N} (\tilde{s}_{uz} - v_6)^4 - 3 \quad (13)$$

v_{10} ranges from -2 to ∞.

As with the GLCM statistics, undefined values, or infinite values, can result for certain descriptive statistics such as skewness and kurtosis when the intensity values in the window are perfectly uniform, that is, when the standard deviation is equal to zero. The value of entropy may also be undefined in the case of pixel intensities having a value of zero in a given distribution. These undefined values are ignored by the SVM classifier. Their influence on the classification accuracy is negligible however as not only do the undefined values tend to appear infrequently, but by having a large feature vector containing a greater number of correctly defined texture measures, their effect is vastly diminished. Moreover, since the sensitivity of each texture measure varies according to the surface type and damage form, having a large feature vector is useful as it ensures that the influence of any texture measures that is ineffective at differentiating between damaged and undamaged regions is offset by other texture features that have a higher sensitivity to regions of contrasting texture.

2.2 Non-linear SVM classification

SVM are used to classify pixels as being either damaged or undamaged, based on the texture feature vector assigned to each pixel. SVM is a supervised learning classifier based on statistical learning theory. The linear SVM is used for linearly separable data using a (*k-1*) dimensional hyperplane in *k*-dimensional feature space (Vapnik, 1995). This hyperplane is called a maximum-margin hyperplane which ensures maximized distance from the hyper plane to the nearest data points on either side in a transformed space. For linearly non-separable data a non-linear SVM is used which relies on kernel function and maximum-margin hyperplane. The kernel function is adopted for non-linear classification instead of the dot product between the data points and the normal vector to the hyperplane as used for the linear classification. The kernel function concept is used to simplify the identification of the hyperplane by transforming the feature space into a high dimensional space

(Boser et al., 1992; Cortes and Vapnik, 1995; Cristianini and Shawe-Taylor, 2000). The hyperplane found in the high dimensional feature space corresponds to a non-linear decision boundary in the input space.

In SVM the classifier hyperplane is generated based on training data sets. Given a training data set of l points in the form $\{(x_h, y_h)\}_{h=1}^{l}$, where h denotes the hth vector in the data set, x_h is a k-dimensional input vector ($x_h \in R^n$), and y_h is an instance label vector ($y_h \in \{1, -1\}^l$); for this study, a value of +1 indicates presence of damage and −1 indicated absence of damage. To identify the maximum-margin hyperplane in the feature space, the SVM requires the solution of the following optimization problem:

$$\{w, e\} = \underset{w,e,\xi}{\arg\min} \left(\tfrac{1}{2} w^T w + C \sum_{h=1}^{l} \xi_h \right); \quad C > 0 \qquad (14)$$
$$\text{subject to } y_h(w^T \varphi(x_h) + e) \geq 1 - \xi_h; \quad \xi_h \geq 0$$

The function φ maps the training vectors x_h into a higher dimensional space. The vector w is the weight vector which is normal to the hyperplane, e is the bias, ξ is the misclassification error, and C is the cost or penalty parameter related to ξ. The solution to the problem is given by

$$\min_{\alpha} \frac{1}{2} \sum_{h=1}^{l} \sum_{q=1}^{l} \alpha_h \alpha_q \, y_h \, y_q \, K(x_h, x_q) - \sum_{h=1}^{l} \alpha_h \qquad (15)$$

With Constraints:

$$\sum_{h=1}^{l} \alpha_h \, y_h = 0$$
$$0 \leq \alpha_h \leq C, \; h = 1, \ldots, l \qquad (16)$$

where K is the kernel function, α is the Lagrange multiplier, q is the index of the input point x_q. The Radial Basis Function (RBF) kernel has been used here,

$$K(x_h, x_q) = \exp\left(-\gamma \left\| x_h - x_q \right\|^2\right), \gamma > 0 \qquad (17)$$

where γ is a kernel parameter. There are two preselected parameter values for the SVM, C and γ. To estimate the optimum parameter values, a novel ROC curve based optimization framework was employed. In this article, the training data set was obtained using texture features from both damaged and undamaged regions in an analyzed image.

2.3 SVM models

Two models were explored to determine the most accurate and efficient approach. The first stage was common to both models and involved training of the SVM with a training set of data. However, the dimensions of the input vectors in the training data sets were different for each model. Also, different implementation methods were carried out in the SVM classification stage. The performance and computational time of each approach was noted.

2.3.1 CWI model. The input vector of each pixel comprises 30 elements: the 10 features stacked together for 3 color channels. A single binary output was achieved by introducing a weighting system which gave a greater prominence to texture measures relating to greater difference between damaged and undamaged regions. The damaged and undamaged zones were identified from the training data. The equation for the weight, W, is as follows:

$$W_{v_f} = \left| \frac{\bar{v}_{f,\,damaged} - \bar{v}_{f,\,undamaged}}{\bar{v}_{f,\,total}} \right| \qquad (18)$$

where $\bar{v}_{f,\,damaged}$ and $\bar{v}_{f,\,undamaged}$ are the averages for the fth texture descriptor in the feature vector for the damaged and undamaged regions in the training data respectively. The average of the overall training data is $\bar{v}_{f,total}$.

The normalized weight, ω_{v_f}, is then assigned to each texture feature, v_f.

$$\omega_{v_f} = \frac{W_{v_f}}{\sum_{v_f} W_{v_f}} \qquad (19)$$

A fundamental issue with the CWI model was that it required 30 separate applications of SVM classifier, one for each of the 10 texture features in each of the three color channels. This does not represent the most effective approach in terms of computational time. However, the weighting system was found to be quite successful in terms of classification accuracy.

2.3.2 4DIS model. The other model considered a 4D input space where the feature vector and the color channels create two dimensions along with image coordinates for the remaining two dimensions. The SVM is applied once to separate the 4D input space into damaged and undamaged segments using a cubical space. It was found that this approach offered the fastest classification time with comparable classification accuracy to the CWI model.

2.4 Performance indicators

The performance of the texture analysis based detection in conjunction with each of the SVM models is evaluated by plotting performance points as a coordinate in the ROC space where the Detection Rate (DR) and the Misclassification Rate (MCR) are the vertical and horizontal coordinates respectively (Rouhan and

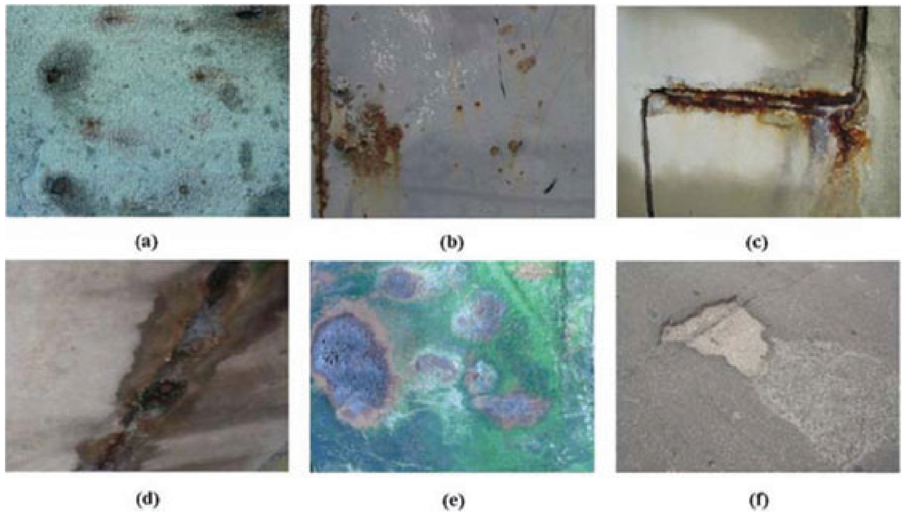

Fig. 3. Sample images in the RGB color space: (a) pitting corrosion on metal sheet piling, (b) corroded metal sheeting, (c) corrosion at a half joint, (d) staining through bridge deck, (e) marine growth on underwater steel surface, (f) exposed bridge deck through pavement.

Schoefs, 2003; Schoefs et al., 2009). The DR and MCR are represented as a percentage between 0% and 100%. The DR and MCR are defined as:

$$DR \approx \frac{Card(Q)}{n_c} \text{ with } Q = \{g \in \Im;\ y_k = 1\} \quad (20)$$

$$MCR \approx \frac{Card(T)}{n} \text{ with } T = \{g \in \Im;\ y_k = -1\} \quad (21)$$

where *Card(.)* indicates the cardinality of a particular set, $\Im = \{1, \ldots, n\}$, n_c denotes the number of corroded pixels, and T gathers situations of incorrectly detected pixels and undetected corroded pixels although Q gathers the correctly detected ones. The ROC space provides a common and convenient tool for graphically characterizing the performance of NDT techniques and its usage has been extended to image detection (Pakrashi et al., 2010). A box counting approach (O'Byrne et al., 2011) was employed to calculate n_c for each image in each color space. The DR and the MCR values formed the basis of selecting the performance point in the ROC space employing the α-δ method (Baroth et al., 2011; Schoefs et al., 2012b). This method relies on calculating the angle, α, and the Euclidean distance, δ, between the best performance point and the considered point to give a measure of the performance of the NDT associated with the point under consideration. The best performance point is defined as an ideal NDT with 100% detection and 0% misclassification rates and represented in the ROC space with coordinates (0,100). For the current article the δ parameter alone may be used for comparison. A low value for δ is indicative of a strong performing technique.

3 EVALUATION OF PROPOSED SEGMENTATION TECHNIQUE

The proposed segmentation technique was applied on six images of various forms of damage on the surface of infrastructural elements. To assess the robustness of the technique, the six images were chosen to reflect a broad range of surfaces, damage forms, viewing angles, lighting conditions, and image resolutions as shown in Figure 3. The sample images in the figure depict, (a) pitting corrosion on metal sheet piling in marine conditions, (b) corroded metal sheeting in coastal regions, (c) corrosion at a half joint on bridge span, (d) staining through bridge deck shown from underneath, (e) marine growth on the surface of underwater steel pile wharf, and (f) exposed concrete bridge deck through wear of pavement surfacing; all in RGB color space. The sample images are shown in HSV and $L^*a^*b^*$ in Figures 4 and 5, respectively. The technique was performed on the images in all three color spaces (RGB, HSV and $L^*a^*b^*$) so as to determine whether a particular color space offered a superior level of performance.

3.1 Results

The following subsections present the results obtained from the CWI and 4DIS models for each color space. The final subsection details the procedure for selecting the SVM parameters: the penalty parameter of the error term, C, and the kernel parameter, γ, so as to optimize the classification accuracy.

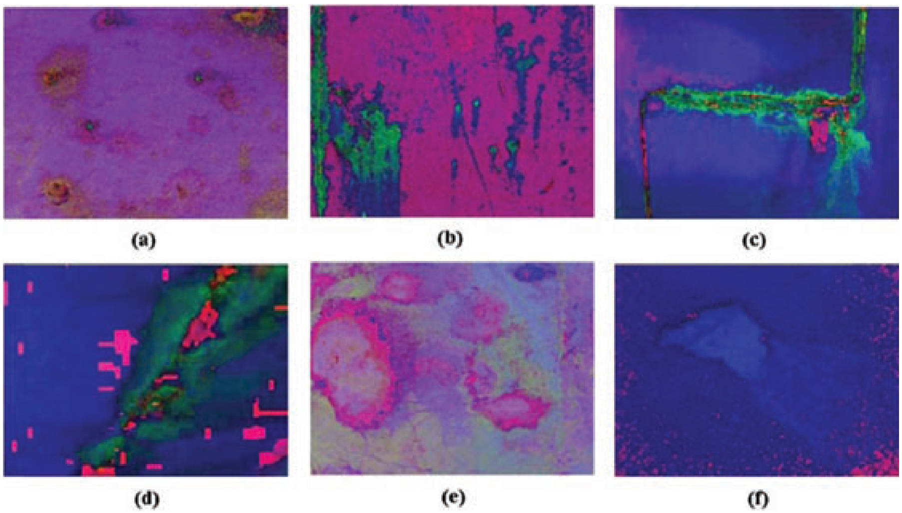

Fig. 4. Sample images in the HSV color space.

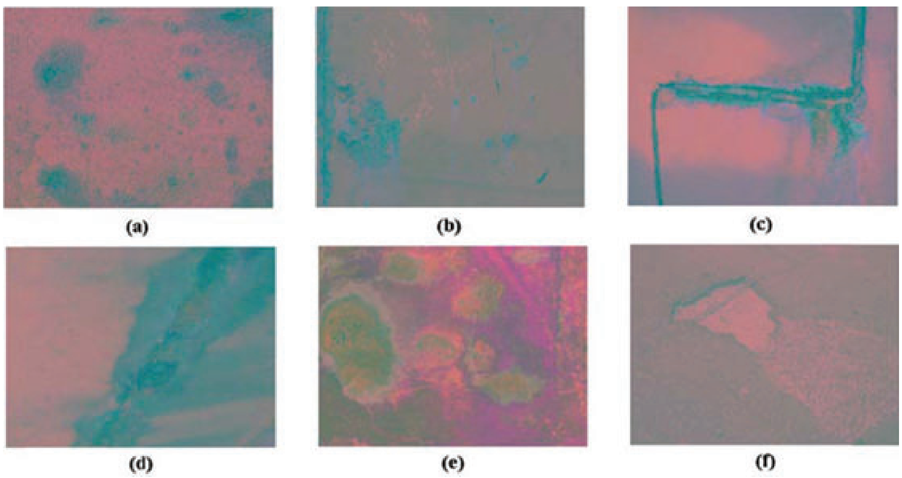

Fig. 5. Sample images in the $L^*a^*b^*$ color space.

3.1.1 CWI model. The detected regions using the CWI model are shown for each color space in Figures 6–8. The detection and misclassification rates are summarized in Table 1. The CWI model performed well in terms of identifying the locations of the damaged regions in the sample images. However, these regions were often poorly defined in many instances, resulting in reduced DR. An example of this is Figure 6c, where the damaged regions in the RGB space have been located, but the identified damage is not homogeneous and the outer boundaries of the damaged areas are inadequately identified. This problem is also observed in the other color spaces.

The classification accuracy was found to be dependent on color space. The δ values in Table 1 provide a quantitative measure of the variation in classification accuracy among color spaces. HSV color space achieved a high level of performance on a consistent basis although the RGB and $L^*a^*b^*$ color spaces were prone to more varied performance levels. The DR values for the sample images in $L^*a^*b^*$ space were generally high but were accompanied with a high MCR as well. The images in RGB color space on the other hand showed moderate DR and high MCR values.

Although the HSV color space generally outperformed the RGB and $L^*a^*b^*$ color spaces, a notable exception to this was in the case of image (f) which produced the best result in the $L^*a^*b^*$ color space. The L^*, or lightness, plane in $L^*a^*b^*$ is essentially the original image with the color data reduced to certain shades of grey only. The L^* plane typically responded well to feature extraction by means of statistical analysis. Conversely, extracting textural features through statistical analysis in the a^* and b^* planes in $L^*a^*b^*$

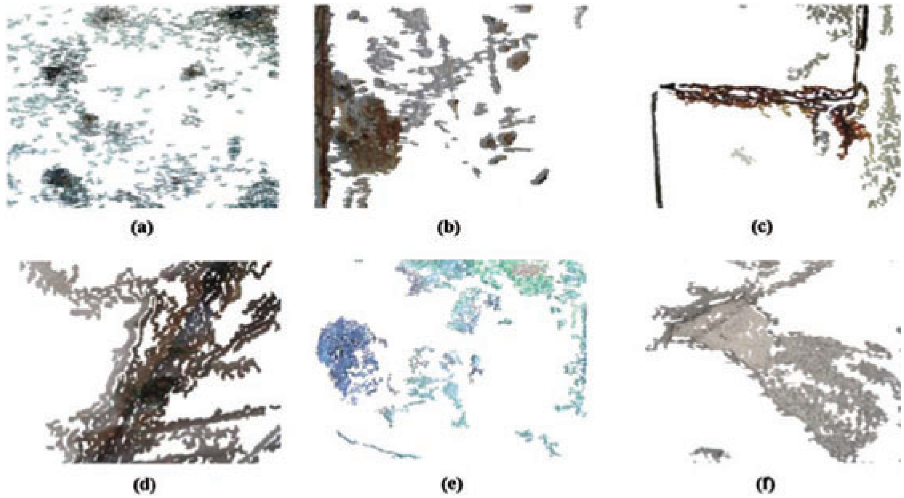

Fig. 6. Detected regions using the CWI model for the RGB color space.

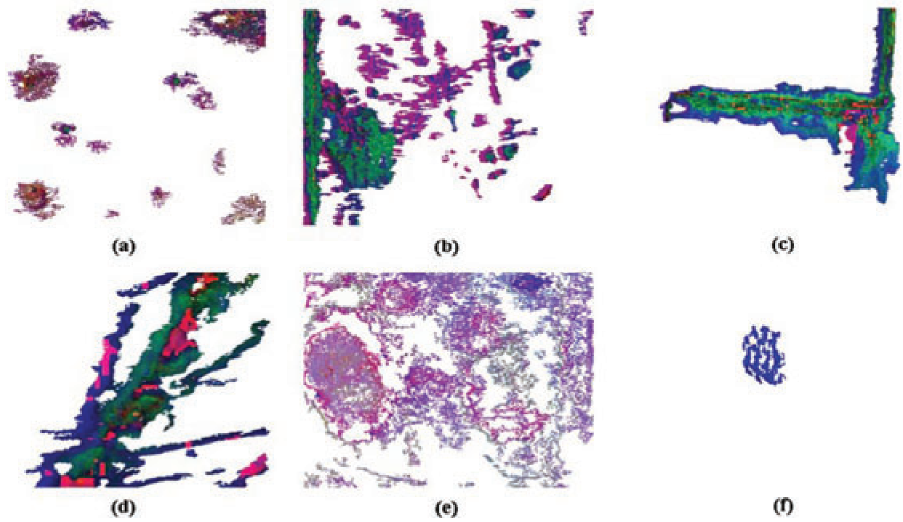

Fig. 7. Detected regions using the CWI model for the HSV color space.

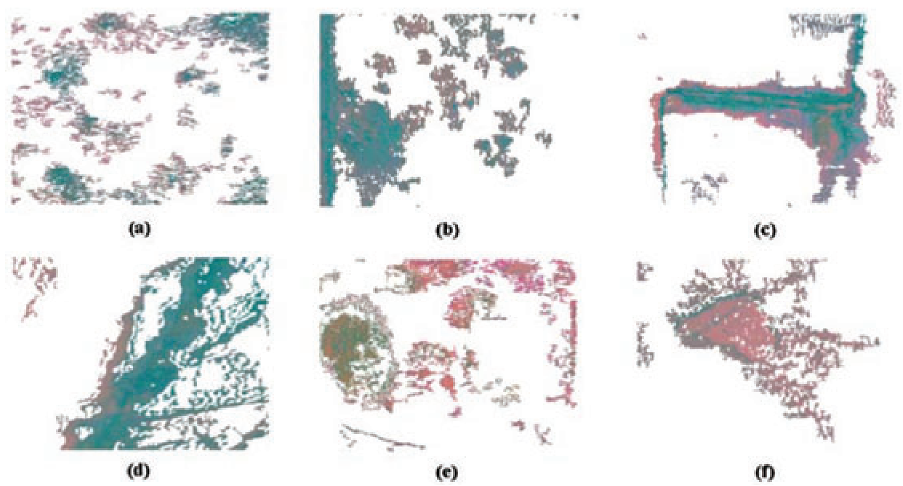

Fig. 8. Detected regions using the CWI model for the $L^* a^* b^*$ color space.

Table 1
Performance for the six images in each color space using the CWI model

	Color space								
	RGB			*HSV*			*$L^*a^*b^*$*		
Sample image	*DR*	*MCR*	δ	*DR*	*MCR*	δ	*DR*	*MCR*	δ
(a) Pitting corrosion	83.96%	30.89%	0.35	84.30%	7.20%	0.17	85.50%	34.64%	0.38
(b) Corroded metal	96.31%	19.69%	0.20	98.00%	20.10%	0.20	94.05%	25.99%	0.27
(c) Half-joint damage	70.82%	10.77%	0.31	94.65%	11.98%	0.13	99.96%	23.23%	0.23
(d) Stained deck	83.57%	36.44%	0.40	79.49%	23.50%	0.31	80.58%	26.10%	0.33
(e) Marine growth	70.16%	40.48%	0.50	43.80%	20.93%	0.60	43.25%	20.12%	0.60
(f) Exposed deck	66.61%	29.05%	0.44	54.38%	6.06%	0.46	73.85%	9.09%	0.28

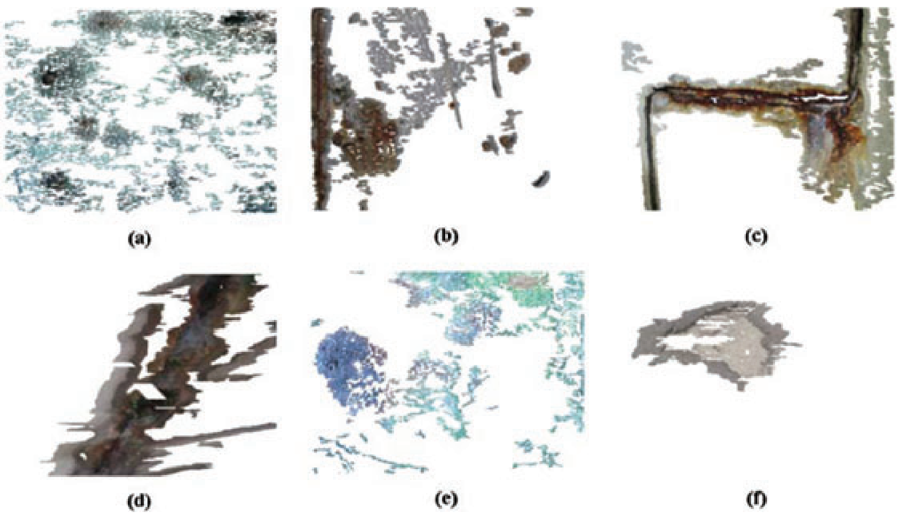

Fig. 9. Detected regions using the 4DIS model for the RGB color space.

generally yielded quite poor results as it was found that these planes were relatively nondescript and offered little distinction between damaged and undamaged regions in terms of texture. As a consequence, the CWI model had to rely disproportionately on the texture descriptors in the L^* plane to obtain a reasonable result. However, this issue was largely offset in the case of image (f) as the dominant colors in the image were varying shades of grey resulting in the L^* plane containing a high proportion of the original image data. As a result, this image was largely unaffected by the poor performances of the statistical analysis in a^* and b^* planes.

The explanation for the poor performance in the RGB color space may be attributed to the high correlation between its RGB components (Cheng et al., 2001). The pixel intensities from the Red, Green, and Blue color channels are all correlated as they contain the same light and contrast information as received by the scene. Hence, the image descriptions in terms of these components make discriminating damaged and undamaged regions difficult. Descriptions in terms of hue-saturation-brightness are often more distinct and therefore more relevant for detection purposes, a point reinforced by the good results attained from the six sample images in the HSV color space.

3.1.2 4DIS model. The detected regions for the 4DIS are shown for each color space in Figures 9–11. The detection and misclassification rates are summarized in Table 2. The 4DIS model succeeded at defining the damaged regions to a better extent than the CWI model. In the majority of the cases, there were only a few spurious regions that were misclassified as being damaged. However, there were occasional cases where comparatively large portions of undamaged regions in the images were misclassified such as in Figure 10f and Figure 11a. As with the CWI model, the performance levels varied significantly between the color spaces. The HSV color space was deemed as the best option. The slightly worse performances in the RGB and $L^*a^*b^*$

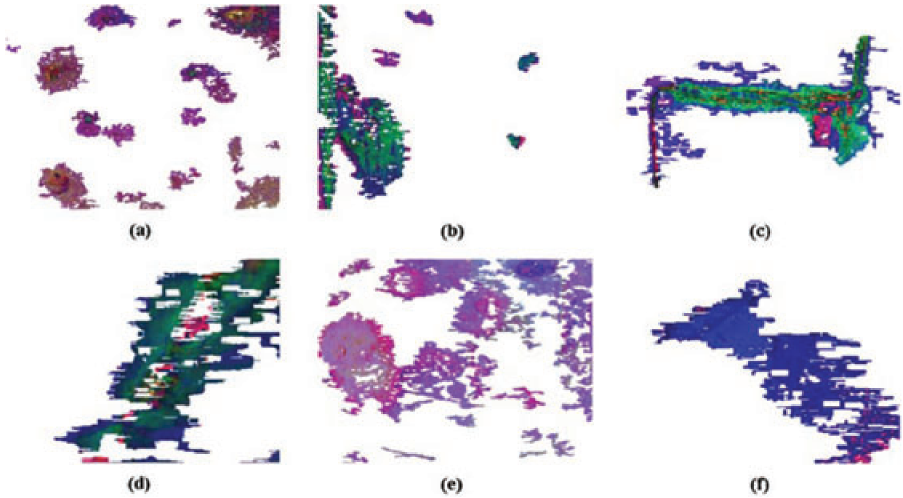

Fig. 10. Detected regions using the 4DIS model for the HSV color space.

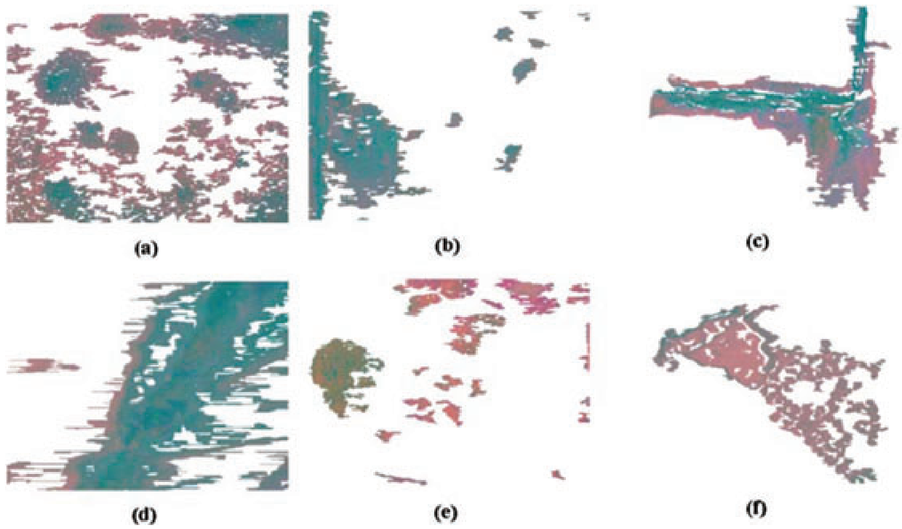

Fig. 11. Detected regions using the 4DIS model for the $L^*a^*b^*$ color space.

color spaces may be attributed to the same reasons as outlined for the CWI model.

3.2 Comparison of model performances

A graphical comparison of the models for each image and color space is provided in Figure 12, in which the performance points corresponding to each model–color space combination are plotted in the ROC space.

To ensure comparability between the CWI and 4DIS model, the same training data were used for each model and color space. Of the six images tested in each color space, the 4DIS model outperformed the CWI model in 61% of cases. However, the performance of the models varied from image to image, with some images responding better to classification via CWI although the other images attained comparatively better results with the 4DIS model (Figure 12).

Both the models performed consistently in different color spaces and the HSV color space typically provided the best results. It is evident in Figure 12, where the performance points corresponding to the HSV color space for both the CWI and 4DIS models are far closer to the best performance point as compared to the other points in the ROC space. The RGB color space used in conjunction with the 4DIS model and the $L^*a^*b^*$ color space used with both the CWI and 4DIS models achieved similar performance levels, reflected by the δ values for a given image in these color space–model combinations. The images in the RGB color space analyzed using the CWI model showed the poorest performance accuracy although the images in the HSV

Table 2
Performance for the six images in each color space using the 4DIS model

	Color space								
	RGB			*HSV*			*L*a*b**		
Sample image	*DR*	*MCR*	δ	*DR*	*MCR*	δ	*DR*	*MCR*	δ
(a) Pitting corrosion	77.78%	32.04%	0.39	88.66%	10.47%	0.15	89.92%	30.22%	0.32
(b) Corroded metal	95.92%	24.14%	0.24	80.25%	9.95%	0.22	86.10%	14.69%	0.2
(c) Half joint damage	94.69%	25.91%	0.26	92.45%	8.02%	0.11	83.22%	10.96%	0.2
(d) Stained deck	71.43%	19.35%	0.35	67.19%	22.96%	0.4	53.27%	16.05%	0.49
(e) Marine growth	64.11%	28.96%	0.46	67.89%	22.45%	0.39	43.49%	15.98%	0.59
(f) Exposed deck	52.06%	10.11%	0.49	86.47%	23.72%	0.27	96.70%	36.21%	0.36

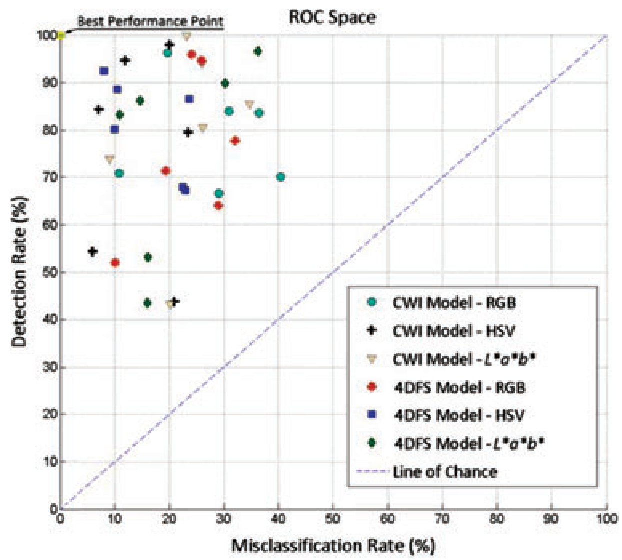

Fig. 12. Performance points in the ROC space showing the performance of the classification models in each color space for images a–f.

color space analyzed using 4DIS model achieved the best performance accuracy.

3.3 Computation times of models

Whilst both models produced apparently comparable classification accuracy, their respective computational times provide a conclusive source of differentiation, with the 4DIS model being the superior option. The computation times for all sample images in RGB space for both models are presented in Table 3 for illustrative purposes. The other color spaces demonstrate similar results. The different computation times for the sample images can be attributed to the image size.

A significant portion of the time in the CWI model may be attributed to its weighting system, which is required to calculate the dissimilarity between texture features in the damaged and undamaged zones, along with the inefficient application of the SVM classifier which is required to be iteratively performed for 30 times.

Table 3
Classification times for the 4DIS and CWI models

		Time taken (seconds)	
Image	*Image size (sq pixels)*	*4DIS model*	*CWI model*
(a) Pitting corrosion	1,056×1,408	46.5	893.6
(b) Corroded metal	635×846	12.6	322.3
(c) Half joint damage	436×648	6.5	130.6
(d) Stained deck	441×427	3.0	97.6
(e) Marine growth	1,056×1,408	51.5	875.2
(f) Exposed bridge deck	255×391	2.5	47.0

3.4 Parameters of the SVM classifier

SVM classification requires a penalty parameter of the error term, C, and the kernel parameter, γ, which define the decision boundary. The parameters should be chosen carefully to produce an effective classifier. An ROC based optimization framework was adopted through which the two components were independently optimized (Schoefs et al., 2012a). Whilst theoretically it would be preferable to search for the optimum (C, γ) pairing, it was found experimentally that this exhaustive and computationally intensive approach was largely unnecessary as the C and γ values were largely independent of each other. For illustrative purposes, the performances of various C and γ values for Figure 3a, analyzed through the 4DIS model, are presented in Tables 4 and 5 respectively. The corresponding ROC curves are displayed in Figures 13a and b, respectively.

The δ values attained for the set of parameter values trialled indicate that the optimum values for C

Table 4
Performance of SVM for various C values (γ kept constant at 1)

C-value	*DR*	*MCR*	δ
0.001	57.00%	11.88%	0.45
0.25	67.90%	17.65%	0.37
0.5	70.20%	20.20%	0.36
0.75	74.90%	26.92%	0.37
1	77.80%	31.90%	0.39
10,000	77.61%	33.13%	0.40

Table 5
Performance of SVM for various γ values (C kept constant at 0.5)

γ-value	*DR*	*MCR*	δ
0.25	39.72%	6.24%	0.61
0.5	57.24%	10.65%	0.44
0.66	62.45%	13.72%	0.40
0.75	64.44%	15.44%	0.39
0.8	66.14%	16.74%	0.38
1	70.28%	20.22%	0.36
1.33	77.74%	31.45%	0.39
2	86.79%	53.83%	0.55

and γ were 0.5 and 1, respectively. It was found that combining these independently optimized parameters provided satisfactory results, with negligible differences from that of the jointly optimized (C,γ) pair. Moreover, the classifier demonstrated a low sensitivity to deviations from the optimal pairing suggesting that a highly optimized pairing was not integral to the classifier performance. This was especially true for the penalty parameter, C, which returned similar performance levels across a range spanning multiple orders of magnitude.

4 CONCLUSION

This article presents a semi-automatic texture analysis based technique for the detection and classification of damaged regions on the surface of infrastructural elements. The technique involves generating a texture feature vector for each pixel in the image including information derived from GLCM based on a quantized grey-level scale along with statistical and energy information from the pixel intensity values. The pixels are consequently classified through non-linear SVM models.

The proposed technique has a number of favorable aspects:

1. Each pixel is qualified through a large feature vector containing ten texture related measures representing both grey-levels and pixel intensities in appropriate scales providing a well-rounded description of the image in terms of the textural characterizing. This aspect also increases the robustness of the technique as some measures may be good at differentiating regions in one image and may not necessarily be particularly useful in another image. This robustness is showcased by the ability of the technique to perform effectively when applied to images featuring a broad range of surfaces and damage forms, exposed to various lighting conditions, viewing angles, and resolutions.
2. The technique is more immune to variations in lighting conditions than color based techniques, where only the pixel intensity values are considered as opposed to texture based segmentation techniques in which the relationship between adjacent pixel intensity values are considered. This relationship is often maintained to a significant extent even when inherent chromatic and luminous complexities are introduced to the scene.

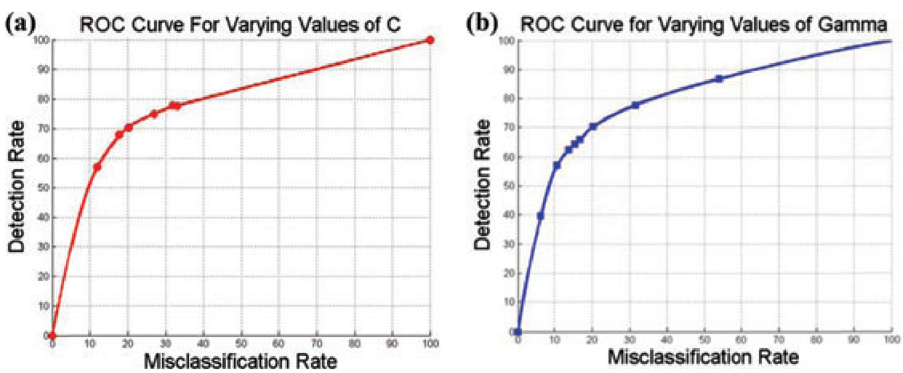

Fig. 13. (a) ROC curve for varying values of C (γ kept constant at 1). (b) ROC curve for varying values of Gamma (C kept constant at 0.5).

3. The technique requires only three parameters to be optimized: the size of the sliding window and two SVM parameters. A ROC curve-based optimization framework has been presented which shows a simple means of attaining suitable values for the SVM parameters. The size of window can be independently chosen through trial-and-error.

Two SVM classification models have been explored: a CWI model and a 4DIS model. The CWI model employed a weighting scheme based on the relative differences of textural descriptors in the damaged and undamaged training data. The SVM was applied iteratively to each texture measure in each color channel. The 4DIS model offered a more efficient approach, requiring only one application of the SVM. The 4DIS model had the fastest computational time and, overall, achieved slightly better classification accuracy over the CWI model.

The proposed technique was performed in RGB, HSV, and $L^*a^*b^*$ color spaces. The HSV color space, in conjunction with the 4DIS model, offered a consistently high level of performance in a time efficient manner, and is thus concluded to be the best combination.

ACKNOWLEDGMENT

The authors wish to thank the Irish Research Council for Science, Engineering and Technology (IRCSET) for providing a grant to support this research and CAPACITES/IXEAD society for the practical and financial assistance.

REFERENCES

Abbiramy, V. S. & Tamilarasi, A. (2011), A comparative study on human spermatozoa images classification with artificial neural network based on FOS, GLCM and morphological features, in D. Nagamalai, E. Renault, & M. Dhanuskodi (eds.), *Proceedings of the Advances in Digital Image Processing and Information Technology*, Communications in Computer and Information Science, Springer, Berlin, Heidelberg, pp. 220–8.

Adeli, H. & Jiang, X. (2009), *Intelligent Infrastructure–Neural Networks, Wavelets, and Chaos Theory for Intelligent Transportation Systems and Smart Structures*, CRC Press, Taylor & Francis, Boca Raton, FL.

Adewuyi, A. P. & Wu, Z. (2011), Vibration-based damage localization in flexural structures using normalized modal macrostrain techniques from limited measurements, *Computer-Aided Civil and Infrastructure Engineering*, **26**(3), 154–72.

Agin, G. J. (1980), Computer vision systems for industrial inspection and assembly, *Computer*, **13**, 11–20.

Baroth, J., Breysse, D. & Schoefs, F. (2011), *Construction Reliability*. Wiley, Hoboken, NJ.

Belli, K., Wadia-Fascetti, S. & Rappaport, C. (2008), Model based evaluation of bridge decks using ground penetrating radar, *Computer-Aided Civil and Infrastructure Engineering*, **23**, 3–16.

Ben Salem, Y. & Nasri, S. (2010), Automatic recognition of woven fabrics based on texture and using SVM, *Signal, Image and Video Processing*, **4**, 429–34.

Boser, B. E., Guyon, I. M. & Vapnik, V. N. (1992), A training algorithm for optimal margin classifiers, in *Proceedings of the Fifth Annual Workshop on Computational Learning Theory*, ACM, Pittsburgh, PA, USA, pp. 144–52.

Cheng, H. D., Jiang, X. H., Sun, Y. & Wang, J. (2001), Color image segmentation: advances and prospects. *Pattern Recognition*, **34**, 2259–81.

Choi, B., Han, S., Chung, B. & Ryou, J. (2011), Human body parts candidate segmentation using laws texture energy measures with skin color, in *Proceedings of the 13th International Conference on Advanced Communication Technology: Smart Service Innovation through Mobile Interactivity*, International Conference on Advanced Communication Technology, ICACT, February 13, 2011–February 16, 2011, Institute of Electrical and Electronics Engineers Inc., pp. 556–60.

Cord, A. & Chambon, S. (2011), Automatic road defect detection by textural pattern recognition based on AdaBoost, *Computer-Aided Civil and Infrastructure Engineering*, **27**(4), 244–59.

Cortes, C. & Vapnik, V. (1995), Support-vector networks. *Machine Learning*, **20**, 273–97.

Cristianini, N. & Shawe-Taylor, J. (2000), *An Introduction to Support Vector Machines and Other Kernel-Based Learning Methods*, Cambridge University Press.

Cruz, P. J. S. & Salgado, R. (2009), Performance of vibration-based damage detection methods in bridges, *Computer-Aided Civil and Infrastructure Engineering*, **24**(1), 62–79.

Cusson, D., Lounis, Z. & Daigle, L. (2011), Durability monitoring for improved service life predictions of concrete bridge decks in corrosive environments, *Computer-Aided Civil and Infrastructure Engineering*, **26**(7), 524–41.

Gadelmawla, E. S. (2004), A vision system for surface roughness characterization using the gray level co-occurrence matrix, *NDT and E International*, **37**, 577–88.

Gallwey, T. J. & Drury, C. G. (1986), Task complexity in visual inspection, *Human Factors: The Journal of the Human Factors and Ergonomics Society*, **28**, 595–606.

Gangone, M. V., Whelan, M. J. & Janoyan, K. D. (2011), Wireless monitoring of a multispan bridge superstructure for diagnostic load testing and system identification, *Computer-Aided Civil and Infrastructure Engineering*, **26**(7), 560–79.

Gill, R. S. (1999), Ice cover discrimination in the Greenland waters using first-order texture parameters of ERS SAR images, *International Journal of Remote Sensing*, **20**, 373–85.

Haralick, R. M., Shanmugam, K. & Dinstein, I. H. (1973), Textural features for image classification, *IEEE Transactions on Systems, Man and Cybernetics*, **3**, 610–21.

Iyer, S. & Sinha, S. K. (2006), Segmentation of pipe images for crack detection in buried sewers, *Computer-Aided Civil and Infrastructure Engineering*, **21**(6), 395–410.

Iyer, S. R., Sinha, S. K. & Schokker, A. J. (2005), Ultrasonic C-Scan imaging of post-tensioned concrete bridge structures for detection of corrosion and voids, *Computer-Aided Civil and Infrastructure Engineering*, **20**(2), 79–94.

Jafarkhani, R. & Masri, S. F. (2011), Finite element model updating using evolutionary strategy for damage detection, *Computer-Aided Civil and Infrastructure Engineering*, **26**(3), 207–24.

Kim, J. H. & Kwak, H.-G. (2008), Nondestructive evaluation of elastic properties of concrete using simulation of surface waves, *Computer-Aided Civil and Infrastructure Engineering*, **23**(8), 611–24.

Komorowski, J. P. & Forsyth, D. S. (2000), Role of enhanced visual inspections in the new strategy for corrosion management, *Aircraft Engineering and Aerospace Technology*, **72**, 5–13.

Lajnef, N., Rhimi, M., Mhamdi, L., Chatti, K. & Faridazar, F. (2011), Toward a smart, long-term pavement monitoring system. *Computer-Aided Civil and Infrastructure Engineering*, **26**(7), 513–23.

Li, H., Huang, Y., Chen, W. L., Ma, M. L., Tao, D. W. & Ou, J. P. (2011a), Estimation and warning of fatigue damage of FRP stay cables based on acoustic emission techniques and fractal theory, *Computer-Aided Civil and Infrastructure Engineering*, **26**(7), 500–12.

Li, H., Huang, Y., Ou, J. & Bao, Y. (2011b), Fractal dimension-based damage detection method for beams with a uniform cross-section. *Computer-Aided Civil and Infrastructure Engineering*, **26**(3), 190–206.

Lu, C. S., Chung, P. C. & Chen, C. F. (1997), Unsupervised texture segmentation via wavelet transform. *Pattern Recognition*, **30**, 729–42.

Mei, X., Gunaratne, M., Lu, J. J. & Dietrich, B. (2004), Neural network for rapid depth evaluation of shallow cracks in asphalt pavements. *Computer-Aided Civil and Infrastructure Engineering*, **19**(3), 223–30.

Nishikawa, T., Yoshida, J., Sugiyama, T. & Fujino, Y. (2012), Concrete crack detection by multiple sequential image filtering, *Computer-Aided Civil and Infrastructure Engineering*, **27**(1), 29–47.

Nugent, M. J. & Pellegrino, B. A. (1991), Remote visual testing (RVT) for the diagnostic inspection of feedwater heaters. in *Proceedings of the 1991 International Joint Power Generation Conference, October 6, 1991—October 10, 1991*, American Society of Mechanical Engineers (ASME), Nuclear Engineering Division (Publication), pp. 55–62.

O'Byrne, M., Pakrashi, V., Ghosh, B. & Schoefs, F. (2011), Receiver operating characteristics of a modified edge detection for corrosion classification, in *Proceedings of the Forum Bauinformatik 23rd European Conference*, Cork, Ireland.

Pakrashi, V., Schoefs, F., Memet, J. B. & O'Connor, A. (2010), ROC dependent event isolation method for image processing based assessment of corroded harbour structures, *Structure and Infrastructure Engineering*, **6**, 365–78.

Park, H. S., Lee, H. M., Adeli, H. & Lee, I. (2007), A new approach for health monitoring of structures: terrestrial laser scanning, *Computer-Aided Civil and Infrastructure Engineering*, **22**(1), 19–30.

Rong-Yau, H., Mao, I. S. & Hao-Kang, L. (2010), Exploring the deterioration factors of RC bridge decks: a rough set approach, *Computer-Aided Civil and Infrastructure Engineering*, **25**(7), 517–29.

Rouhan, A. & Schoefs, F., (2003), Probabilistic modelling of inspection results for offshore structures. *Structural Safety*, **25**(4), 379–99.

Sarma, K. C. & Adeli, H. (1998), Cost optimization of concrete structures, *Journal of Structural Engineering*, **124**, 570–78.

Schoefs, F., Abraham, O. & Popovics, J. (2012a), Quantitative evaluation of NDT method performance: application example based on contactless impact echo measurements for void detection in tendon duct, *Construction and Building Materials (CBM)*, In Press. Available online 29 March 2012. doi: /10.1016/j.conbuildmat.2012.02.002.

Schoefs, F., Clément, A. & Nouy, A. (2009), Assessment of spatially dependent ROC curves for inspection of random fields of defects, *Structural Safety*, **31**(5), 67–78.

Schoefs, F., Clément, B. J. & Capra, B. (2012b), The $\alpha\delta$ method for modelling expert judgment and combination of NDT tools in RBI context: application to marine structures, structure and infrastructure engineering: maintenance, management, life-cycle design and performance (NSIE), *Monitoring, Modeling and Assessment of Structural Deterioration in Marine Environments*, **8**, 531–43.

Schoefs, F., Yanez-Godoy, H. & Lanata, F. (2011), Polynomial chaos representation for identification of mechanical characteristics of instrumented structures, *Computer-Aided Civil and Infrastructure Engineering*, **26**(3), 173–89.

Sirca, Jr., G. F. & Adeli, H. (2005), Cost optimization of prestressed concrete bridges, *Journal of Structural Engineering*, **131**, 380–88.

Sohn, H., Kim, S. D. & Harries, K. (2008), Reference-free damage classification based on cluster analysis, *Computer-Aided Civil and Infrastructure Engineering*, **23**(5), 324–38.

Talebinejad, I., Fischer, C. & Ansari, F. (2011), Numerical evaluation of vibration-based methods for damage assessment of cable-stayed bridges, *Computer-Aided Civil and Infrastructure Engineering*, **26**(3), 239–51.

Tsai, Y. & Huang, Y. (2010), Automatic detection of deficient video Log images using a histogram equity index and an adaptive gaussian mixture model, *Computer-Aided Civil and Infrastructure Engineering*, **25**(7), 479–93.

Vapnik, V. N. (1995), *The Nature of Statistical Learning Theory*. Springer-Verlag, New York.

Xia, Y., Ni, Y.-Q., Zhang, P., Liao, W.-Y. & Ko, J.-M. (2011), Stress development of a supertall structure during construction: field monitoring and numerical analysis, *Computer-Aided Civil and Infrastructure Engineering*, **26**(7), 542–59.

Xian, G.-M. (2010), An identification method of malignant and benign liver tumors from ultrasonography based on GLCM texture features and fuzzy SVM. *Expert Systems with Applications*, **37**, 6737–41.

Yusa, N., Janousek, L., Rebican, M., Chen, Z., Miya, K., Chigusa, N., & Ito, H. (2006), Detection of embedded fatigue cracks in Inconel weld overlay and the evaluation of the minimum thickness of the weld overlay using eddy current testing, *Nuclear Engineering and Design*, **236**, 1852–59.